RSC Publishing Faraday Discussions

Quantum Coherence in Ultrafast Photo-driven Charge Separation

Journal:	*Faraday Discussions*
Manuscript ID	FD-ART-11-2018-000218
Article Type:	Paper
Date Submitted by the Author:	30-Nov-2018

Complete List of Authors:	Phelan, Brian; Northwestern University, Department of Chemistry Schultz, Jonathan; Northwestern University, Department of Chemistry Zhang, Jinyuan; Northwestern University, Department of Chemistry Huang, Guan-Jhih; Northwestern University, Department of Chemistry; Taiwan Semiconductor Manufacturing Co Ltd Young, Ryan; Northwestern University, Department of Chemistry Wasielewski, Michael; Northwestern University, Department of Chemistry

Title:

Quantum Coherence in Ultrafast Photo-driven Charge Separation

Authors:

Brian T. Phelan[√], Jonathan D. Schultz[√], Jinyuan Zhang, Guan-Jhih Huang, Ryan M. Young[*], Michael R. Wasielewski[*]

[√]Brian T. Phelan and Jonathan D. Schultz contributed equally

*Correspondence to: m-wasielewski@northwestern.edu, ryan.young@northwestern.edu

Affiliations:

Department of Chemistry and Institute for Sustainability and Energy at Northwestern, Northwestern University, Evanston, IL 60208-3113, USA

Abstract

Coherent interactions are prevalent in photodriven processes, ranging from photosynthetic energy transfer to superexchange-mediated electron transfer, resulting in numerous studies aimed towards identifying and understanding these interactions. A key motivator of this interest is the non-statistical scaling laws that result from coherently traversing multiple pathways due to quantum interference. To that end, we employed ultrafast transient absorption spectroscopy to measure electron transfer in two donor-acceptor molecular systems comprising a *p*-(9-anthryl)-*N*,*N*-dimethylaniline chromophore/electron donor and either one or two equivalent naphthalene-1,8:4,5-bis(dicarboximide) electron acceptors at both ambient and cryogenic temperatures. The two-acceptor compound shows a statistical factor of 2.1 ± 0.2 rate enhancement at room temperature and a non-statistical factor of 2.6 ± 0.2 rate enhancement at cryogenic temperatures, suggesting correlated interactions between the two acceptors with the donor and with the bath modes. Comparing the charge recombination rates indicates that the electron is delocalized over both acceptors at low temperature but localized on a single acceptor at room temperature. These results highlight the importance of shielding the system from bath fluctuations to preserve and ultimately exploit the coherent interactions.

1. Introduction

Extensive work during the past several decades suggests that quantum coherence may play a functional role in various natural and artificial processes,[1] including energy transfer (EnT),[2-6] singlet exciton fission (SF),[7,8] and electron transfer (ET) reactions.[9-16] Much of this evidence manifests as damped oscillations superimposed on population dynamics, or extracted from spectral lineshape analysis, that result from coherent nuclear motion along the Franck-Condon active modes following excitation by a sufficiently short laser pulse.[17] These vibrational wavepackets have lifetimes of 100s of femtoseconds, even in dynamic or disordered environments,[6,7,11,18-23] which can be similar to the timescales of fast excited-state reactions. In some cases, these wavepackets have even been observed to survive reactions, e.g. in SF and ET.[7,11,13,21-23] The timescales for damping of the oscillations, i.e. dephasing of the wavepackets, indicate that the relevant chromophores are not vibrationally relaxing before the reaction, therefore implicating coherence as being functionally relevant to the excited-state reaction.

While the coherences observed in EnT in photosynthetic light harvesting (PS) are believed to be primarily vibrational or vibronic in nature,[5,16,24,25] electronic coherence, in the context of donor-acceptor (DA) electronic coupling, plays a key role in ET reactions occurring via superexchange interactions in donor-bridge-acceptor (DBA) supramolecular architectures and manifests in a variety of ways. Increasing the bridge length has been shown to induce a transition from the coherent superexchange to incoherent hopping mechanism which results from the distance dependences of the bridge state-mediated ET coupling.[26-30] ET rates across norbornyl bridges were shown to be attenuated due to symmetry constraints, i.e. destructive interference, between the electron donor and acceptor orbitals.[31-34] Theoretical and experimental investigations of conductance[35,36] and ET rates[37-39] through conjugated and cross-conjugated bridges demonstrate

marked decreases in coupling element magnitudes for the cross-conjugated systems resulting from destructive interference. More generally, quantum interference between multiple equivalent pathways results in rates that may scale non-statistically with the number of available pathways where constructive and destructive interference lead to ET rate enhancement and suppression, respectively.[40-49] One of the key results of these studies has been determining the role of dephasing, usually resulting from fluctuations in the donor, acceptor, or bridge site energies, with small fluctuations or weak system-bath coupling allowing for longer correlations between bridge sites and therefore preservation of interference effects.

The coherent effects arising from quantum interference between multiple equivalent pathways is particularly interesting for potential molecular electronics applications and since Nature has selected such a topology for the photosynthetic reaction centers (RCs). It is unlikely that the excited electron propagates coherently down both pathways in the RCs since (i) the two pathways are not strongly interacting and (ii) the electron is observed to populate the intermediate chlorophyll and phylloquinone acceptors. However, experimental observations of long-lived vibrational wavepacket dynamics in PS[18,20,50,51] indicate that the protein matrix may work to alleviate sources of dephasing, which may also apply to site fluctuations in the RCs, and theoretical modeling suggests that quantum interference effects are possible.[44] In artificial systems, interest is driven primarily by the potential to enhance or control ET dynamics through use of supramolecular systems with multi-path topologies. Beratan and co-workers have described molecules and experiments where vibrational excitation provides a handle to turn quantum interference on or off,[48] while Rubtsov *et al.* and Weinstein *et al.* have used such experiments for related problems.[52,53] Demonstrating rate enhancement due to constructive interference experimentally is necessary to better understand when it can be utilized to enhance function. However, it is

particularly challenging because the most straightforward method relies upon a comparison between two separate molecular systems, where structural differences can lead to larger enhancements than that from constructive interference.[54] Several groups, however, have demonstrated strong experimental evidence for constructive interference by measuring conductance via STM-break junction experiments[55] and the exchange coupling between two spin centers via electron paramagnetic resonance spectroscopy,[56] with the latter example operating over an impressive 3.9 nm. While these elegant experiments clearly demonstrate constructive interference, neither observes ET dynamics using time-resolved techniques. Though synthesis of full DBA systems featuring one or two equivalent pathways has yet to be realized, here we report on ultrafast charge separation (CS) and nanosecond charge recombination (CR) in two DA molecules containing either one or two equivalent acceptors. The DA architecture studied here also lends itself to closure into a full two-path system. Though the pair of acceptors is found to be highly susceptible to dephasing, the system still demonstrates coherent interactions suggesting it could be used for future studies on ET in closed two-pathway DBA architectures.

2. Experimental

2.1 Synthesis

The full synthetic routes as well as characterization of the intermediates and final products are provided in detail in the supporting information section 2 (SI-2).

2.2 Electrochemistry

Differential pulse voltammetry (DPV) experiments were conducted in argon-purged room temperature solutions in dichloromethane (DCM) using a CH Instruments, Inc. model 660 electrochemical workstation interfaced to a computer. The DPV experiments were performed using Pt as the working and counter electrodes, Ag/AgCl as the reference electrode, and ferrocene

as an internal standard. The concentration of the supporting electrolyte, tetrabutylammonium hexafluorophosphate ($TBAPF_6$) was 0.1 M.

2.3 Optical spectroscopy

Steady-state UV-visible absorption spectra were collected using a Shimadzu UV-1800 spectrophotometer for **1NDI** and **2NDI** prepared as room temperature solutions (less than 1 mM) in 1,4-dioxane with optical densities less than 1.0 in quartz cuvettes with a 1 mm path length. Transient absorption (TA) spectroscopy experiments were performed using a 1 kHz regeneratively-amplified Ti:sapphire laser system (Tsunami oscillator / Spitfire Pro amplifier, Spectra-Physics Inc.) described previously.[57] Briefly, half of the about 80 fs 1 mJ/pulse fundamental was used to seed a commercial non-collinear optical parametric amplifier (TOPAS-White, Light Conversion, LLC) to generate the pump pulse centered at 435 nm, less than 50 fs (Figure S1-3). The pump pulse was directed through an external prism compressor (LaK21 glass) with a 154 mm separation to pre-compensate for second-order dispersion accumulated in transmissive optics and the sample cells. The polarization of the pump pulse was set to magic angle (54.7°) with respect to the probe pulse and attenuated to 300-500 nJ/pulse at the sample. About 5% of the remaining fundamental was directed along a delay stage before about 2 μJ/pulse were focused into a translated CaF_2 crystal (uncoated, 2 mm, <001> cut, Newlight Photonics Inc) to generate the probe pulse. The probe pulse was split so that one portion interacted with the sample and the other provided a reference pulse. The signal and reference probe pulses were coupled into optical fibers and detected using a customized Helios spectrometer and Helios software (Ultrafast Systems, LLC).

TA experiments were performed at room temperature (295 K) and at cryogenic temperatures (90 and 5.5 K). The room temperature samples were prepared as solutions (less than 1 mM) in 1,4-

dioxane in 1 mm quartz cuvettes and were stirred to avoid the effects of local heating and sample degradation. The cryogenic temperature samples were prepared as solutions in 2-methyltetrahydrofuran (Me-THF) in a glove box under nitrogen atmosphere (to exclude oxygen) and sealed between two quartz windows with an about 0.75 mm PTFE o-ring spacer. The sample holder was mounted between two copper plates in an STVP-100 cryostat (Janis Research Company, LLC) and the temperature was controlled with a Cryo-Con 32B temperature controller (Cryogenic Control Systems, Inc). The pump pulse was focused to a diameter of about 500 μm and the cryostat was translated normal to the probe pulse after each scan of the delay stage to minimize the effects of local heating and sample degradation and to average over inhomogeneities in the frozen solution. The instrument response duration of these experiments, τ_{IRF}, defined as the full-width at half-maximum of the Gaussian instrument response function (IRF), reached a minimum of about 90 fs at probe frequencies near that of the pump and increased significantly at probe frequencies further from the pump. Measurements were performed for each sample on three separate days with new samples prepared each day.

2.4 Density functional theory computation

Density functional theory (DFT) calculations were performed at the level of ωB97X-D/6-31G* *in vacuo* using Q-Chem 5.1 to obtain optimized geometries for the neutral, singly reduced, and singly oxidized **1NDI** and **2NDI** (see SI-5).[58] The solubilizing octyl chains bonded to the **NDI** imide nitrogen were replaced with a methylene ($-CH_3$) group to simplify the calculation. Normal mode analyses were completed using the optimized structures at the same level of theory to confirm that no or only one imaginary frequencies were found (Table S1). We then calculated the single-point energies of the singly oxidized and singly reduced **1NDI** and **2NDI** using the

optimized neutral geometries to determine the internal reorganization energy for each sample (*vide infra*).

3. Results and Discussion

3.1 Synthesis

The two DA complexes reported here employ a *p*-(9-anthryl)-*N*,*N*-dimethylaniline moiety (**DMA-An**) as the chromophore and initial electron donor state. We employ naphthalene-1,8:4,5-bis(dicarboximide) (**NDI**) as the electron acceptor bonding either one **NDI** through the imide nitrogen to the 4-position of the anthracene (**An**) moiety in **DMA-An** or two **NDI**s to the 4- and 5-positions of the **An** moiety yielding **1NDI** and **2NDI**, respectively (Figure 1A).

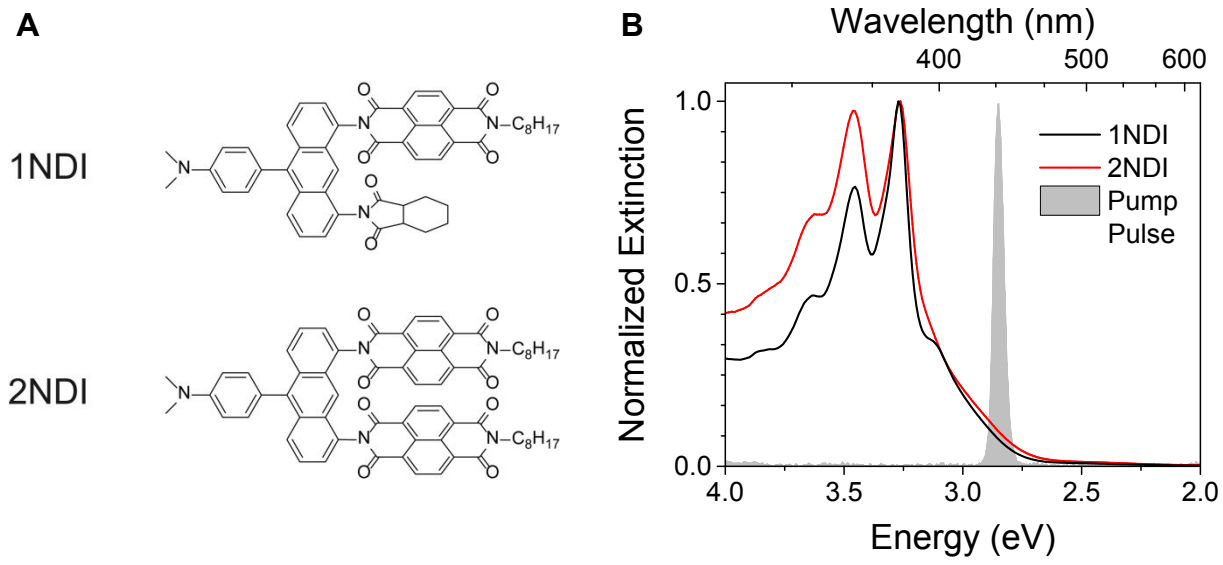

Figure 1. (A) Molecular structures for the compounds in these studies and (B) normalized steady-state absorption spectra obtained in 1,4-dioxane at 295K with the typical excitation pulse spectrum superimposed.

3.2. Steady-state electronic absorption spectroscopy

The normalized electronic absorption spectra of **1NDI** and **2NDI** dissolved in 1,4-dioxane at 295K are shown in Figure 1B. Both compounds display a prominent vibronic progression of

about 1450 cm^{-1} primarily due to the **NDI** moieties with absorption maxima at 3.27, 3.46, and 3.63 eV (379, 358, and 342 nm).[59] The **An** moiety also contributes to the observed absorption maxima, though only weakly as a result of a charge-transfer (CT) interaction with **DMA** which is evidenced by the broad tail extending from the lowest energy vibronic feature to about 2.5 eV (496 nm) in both **1NDI** and **2NDI**.[60] The CT transition only results in partial ET between **DMA** and **An** to yield $\mathbf{DMA^{\delta\bullet+}}$-$\mathbf{An^{\delta\bullet-}}$, especially in low polarity environments where the TA spectra do not resemble a linear combination of the radical ion spectra.[60,61] In **2NDI** compared to **1NDI**, the 3.27 eV vibronic transition decreases in relative absorption with respect to the two higher energy vibronic transitions at 3.46 and 3.63 eV. This results from positive dipolar coupling between the two H-aggregated **NDI** moieties,[62] as has been observed previously for a similar arrangement of **NDI**s.[63]

3.3 Electrochemistry

DPV experiments were conducted on **1NDI** and **2NDI** to determine the reduction and oxidation (redox) potentials for calculation of the CS driving force ΔG_{CS} in each system. Figure 2 shows voltammograms collected for both compounds and values for the measured redox potentials are shown in Figure 2 as well as listed in Table 1. The oxidation potential for **DMA** was observed in both compounds at about 0.9 V vs the saturated calomel electrode (SCE), though it shifted 40 mV more positive in **2NDI** compared to **1NDI**, possibly due to an additional electron withdrawing effect of the second **NDI**. In **1NDI**, two reduction events were observed at -0.54 V and -1.05 V vs SCE corresponding to one electron reductions generating $\mathbf{NDI^{\bullet-}}$ and $\mathbf{NDI^{2-}}$, respectively. In **2NDI**, however, the first reduction wave split by 0.18 mV to yield two similar intensity reduction waves at -0.45 V and -0.63 V vs. SCE which indicates interaction between the lowest unoccupied molecular orbitals (LUMO) on the two **NDI** moieties. The more negative reduction wave shifted

30 mV positive to -1.02 V vs. SCE and would likely show a similar splitting as the less negative reduction wave if more negative potentials were scanned. As the splitting of the reduction waves in **2NDI** is driven by electronic interaction between the two **NDI** moieties, we employed the voltage of the lower energy reduction event for the calculation of ΔG_{CS} in **2NDI**.

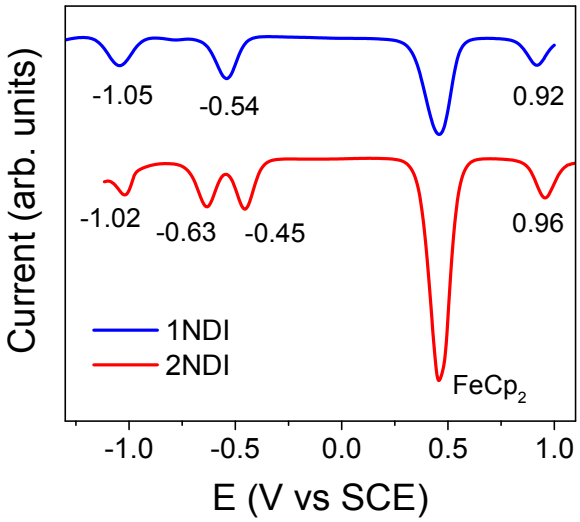

Figure 2. Differential pulse voltammograms of **1NDI** and **2NDI** in DCM with 0.1 M $TBAPF_6$.

3.4 Density functional theory computation and energetic parameters

DFT calculations were performed to obtain optimized geometries for **1NDI** and **2NDI** in the neutral, singly oxidized, and singly reduced states which were used to estimate ΔG_{CS} and the internal reorganization energy λ_v. We conducted normal mode analyses on each system to affirm the validity of the optimized structures as determined by the presence of no or only low frequency, less than 100 cm^{-1}, imaginary modes. While four of these normal mode analyses found either no or only one low frequency imaginary mode (Table S1), two of the analyses were unable to converge under the tight convergence criteria specified (singly oxidized **1NDI** and singly reduced

2NDI). Considering the frequencies of the one imaginary mode found for each of neutral **1NDI** and singly reduced **1NDI** are particularly low, less than 40 cm^{-1}, we assume their contribution to the determined value of λ_v is negligible. Additionally, we note that the 1.0 x 10^{-8} tolerance for convergence used in these calculations, as compared to the more relaxed default 1.0 x 10^{-7} tolerance typically employed, is less likely to yield optimized structures with high frequency imaginary modes.

ΔG_{CS} is the free energy change between the initial donor state and the final radical ion pair (RP) state and can be calculated using Equation 1,[64]

$$\Delta G_{CS} = -E_{00} + e(E_{ox} - E_{red}) - \frac{e^2}{4\pi\varepsilon_0 R_{DA}\varepsilon_s} + \frac{e^2}{4\pi\varepsilon_0}\left(\frac{1}{2r_+} + \frac{1}{2r_-}\right)\left(\frac{1}{\varepsilon_s} - \frac{1}{\varepsilon_{sp}}\right) \qquad \text{Equation 1}$$

where E_{00} is the energy of the initial excited state, E_{ox} and E_{red} are the donor (**DMA**) oxidation and acceptor (**NDI**) reduction potentials, respectively, e is the elementary charge, ε_0 is the permittivity of free space, ε_s is the static dielectric constant of the experimental medium, ε_{sp} is the static dielectric constant of the solvent in which the electrochemical measurements were performed, R_{DA} is the distance between the **DMA**$^{\bullet+}$ and **NDI**$^{\bullet-}$ moieties, and r_+ and r_- are the hard-sphere radii of **DMA**$^{\bullet+}$ and **NDI**$^{\bullet-}$, respectively. r_+ and r_- were assumed to each be equal to half of R_{DA}. ΔG_{CS} values calculated via Equation 1 are provided in Table 1. For these estimates, we assumed E_{00} was equal to the photon energy of the pump pulse since the **DMA**$^{\delta\bullet+}$-**An**$^{\delta\bullet-}$ excited state is known to have complex relaxation dynamics occurring on longer timescales than CS.[65] The estimated ΔG_{CS} values indicated that CS is more favorable for **2NDI** than for **1NDI**, primarily due to the less negative reduction potential.

The reorganization energy λ represents the energy associated with rearranging the system to accommodate the new charge distribution. λ is typically estimated by separately considering the

reorganization energy of the solvent shell λ_S and λ_v which accounts for changes in the intramolecular vibrational modes of the donor and acceptor. λ_S was estimated for the room temperature solutions using the Born continuum model (Equation 2) which treats the solvent as a dielectric continuum where *n* is the refractive index.

$$\lambda_S = \frac{e^2}{4\pi\varepsilon_o}\left(\frac{1}{2r_+} + \frac{1}{2r_-} - \frac{1}{R_{DA}}\right)\left(\frac{1}{n^2} - \frac{1}{\varepsilon_s}\right) \quad \text{Equation 2}$$

At cryogenic temperatures the solvent has frozen and is restricted to small translational motions, so λ_S approaches zero and becomes negligible with respect to λ_v.[66] Therefore, we estimated λ as $\lambda_S + \lambda_v$ at room temperature and λ_v at cryogenic temperatures. The energies determined for the optimized geometries along with single-point energies of the singly reduced and singly oxidized **1NDI** and **2NDI** at the optimized neutral geometries were used to calculate λ_v using Equations 3-4, values for which are given in Table 1.

$$\lambda_v = \lambda_v^+ + \lambda_v^- \quad \text{Equation 3}$$

$$\lambda_v^{+/-} = E_{neutral}^{+/-} - E_{opt}^{+/-} \quad \text{Equation 4}$$

$\lambda_v^{+/-}$ is the internal reorganization energy for oxidation of the donor and reduction of the acceptor, $E_{neutral}^{+/-}$ is the energy of the oxidized donor or reduced acceptor at the neutral geometry, and $E_{opt}^{+/-}$ is the energy of the oxidized donor or reduced acceptor at the optimized geometry. λ_v^+ contributes about 0.4-0.5 eV to the overall λ_v for **1NDI** and **2NDI**, nearly twice that of λ_v^- due to the planarization of the **DMA** moiety upon oxidation. That λ_v^- for **2NDI** is similar to that of **1NDI**, showing only a small increase, is expected regardless of how the electron interacts with the pair of **NDI** acceptors. If the electron is localized, then it interacts with a similar number of normal modes in both **1NDI** and **2NDI** and, if the electron is delocalized, then while it interacts with significantly more modes in **2NDI** compared to **1NDI**, it leads to smaller changes in the modes since the electron

is spread over the additional modes. Comparison of the estimated ΔG_{CS} and λ_v values for each compound indicate that CS is in the Marcus-inverted region at cryogenic temperatures, while at room temperature in 1,4-dioxane CS for **1NDI** is nearly activationless and CS for **2NDI** is slightly inverted.[67] Additionally, between **2NDI** and **1NDI**, the increased exoergicity combined with the decreased reorganization energy for **2NDI**, indicates that CS is slightly further in the inverted region for **2NDI** compared to **1NDI**.

Table 1. Redox potentials in V vs SCE along with donor-acceptor distance, internal reorganization energy, total reorganization energy in 1,4-dioxane, and driving force for charge separation in 1,4-dioxane and glassy Me-THF for **1NDI** and **2NDI**.

	E^+ (V)	E^- (V)	R_{DA} (Å)	λ_v (eV)	λ (eV)[a]	ΔG_{CS} (eV)	
						1,4-dioxane[a]	Me-THF[b]
1NDI	0.92	-0.54	6.65	0.73	0.92	-0.89	-1.03
2NDI	0.96	-0.45	6.51[c]	0.61	0.80	-0.93	-1.08

a. For samples in 1,4-dioxane at 295 K; calculated λ_S using $n = 1.42$ and $\varepsilon_S = 2.22$[68]
b. For samples at 90 and 5.5 K; calculated using $\varepsilon_S = 2.6$[69]
c. Assumes the negative charge distribution is centered between both **NDI** moieties

3.5 Transient electronic absorption spectroscopy

3.5.1 Charge separation dynamics

TA spectra were recorded following excitation of the **DMA-An** CT transition with a 435 nm, 50 fs pump pulse which, as discussed above, generates the polar singlet excited state with partial ET **DMA$^{\delta\bullet+}$-An$^{\delta\bullet-}$**. The TA spectra of **1NDI** following excitation at 435 nm are shown in Figure 3A-C for solutions in 1,4-dioxane at 295 K and Me-THF at 90 and 5.5 K, respectively. At all the temperatures studied here, the transient spectrum of **DMA$^{\delta\bullet+}$-An$^{\delta\bullet-}$** is either only briefly observed (295 K) or obscured due to sub-picosecond evolution of the TA spectra. Figure 3A shows, at time delays immediately following the cross-phase modulation, negative absorption at 405 and 380 nm,

assigned to ground state bleach (GSB) features of the CT transition and localized **An** transition, respectively, and positive absorption at 590 and 340 nm assigned to excited-state absorption (ESA) from **DMA**$^{\delta\bullet+}$-**An**$^{\delta\bullet-}$ to higher lying singlet excited states S_n.[61] These features, except for the 405 nm GSB, decay rapidly yielding new negative features at 378 and 357 nm, assigned as GSB of the **NDI**-localized absorption, and new positive ESA features at 475, 585, 607, 632, and 697 nm. The ESA at 475, 607, and 697 nm indicate formation of **NDI**$^{\bullet-}$.[59] The 585, 632, and 697 nm ESA closely resemble the steady-state electronic absorption spectrum measured for **DMA-An** dissolved in 2-chlorobutane following photolysis with 355 nm light (Figure S5). We assign these transitions to ESA of **DMA**$^{\bullet+}$. Notably, the 405 nm GSB does not decay rapidly with the other initial TA features, as is expected for the CT transition. Formation of the **NDI**$^{\bullet-}$ and **DMA**$^{\bullet+}$ ESA along with GSB of **NDI** and the CT transition provide clear evidence of rapid CS yielding **DMA**$^{\bullet+}$-**An**-**NDI**$^{\bullet-}$. Similar dynamics are observed for **1NDI** dissolved in Me-THF at 90 and 5.5 K with CS still occurring on the sub-picosecond timescale.

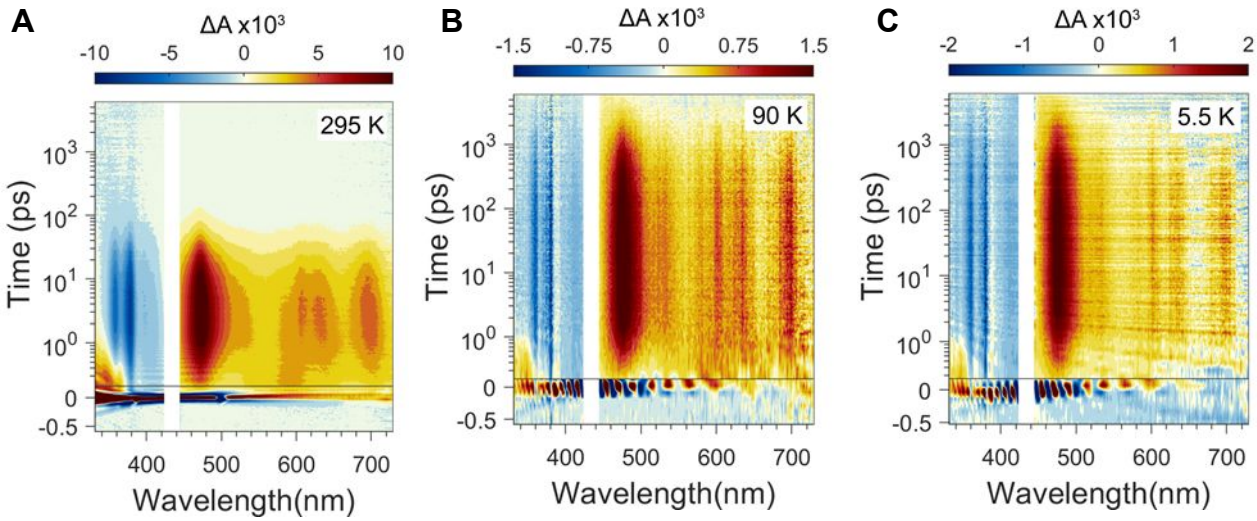

Figure 3. TA spectra of **1NDI** in (A) 1,4-dioxane at 295K, (B) glassy Me-THF at 90K, and (C) glassy Me-THF at 5.5K. Upper and lower sections of each plot are displayed with logarithmic and linear scales, respectively. Pump scatter is blocked for clarity.

The TA spectra of **2NDI** following direct CT excitation under identical experimental conditions as **1NDI** are provided in Figure 4. The signals observed for this compound parallel those described for **1NDI** apart from changes in the relative ESA band amplitudes. In contrast to the **NDI**$^{\bullet-}$ ESA features, absorption by **DMA**$^{\bullet+}$ in the **2NDI** compound is more intense compared to that in **1NDI** under all measured conditions. Moreover, comparison of Figures 3 and 4 shows differences in the kinetics of species generated by CS in **1NDI** and **2NDI**. Namely, the anionic and cationic ESA features imply more rapid formation of **DMA**$^{\bullet+}$**-An-NDI**$^{\bullet-}$ in **2NDI** than **1NDI**.

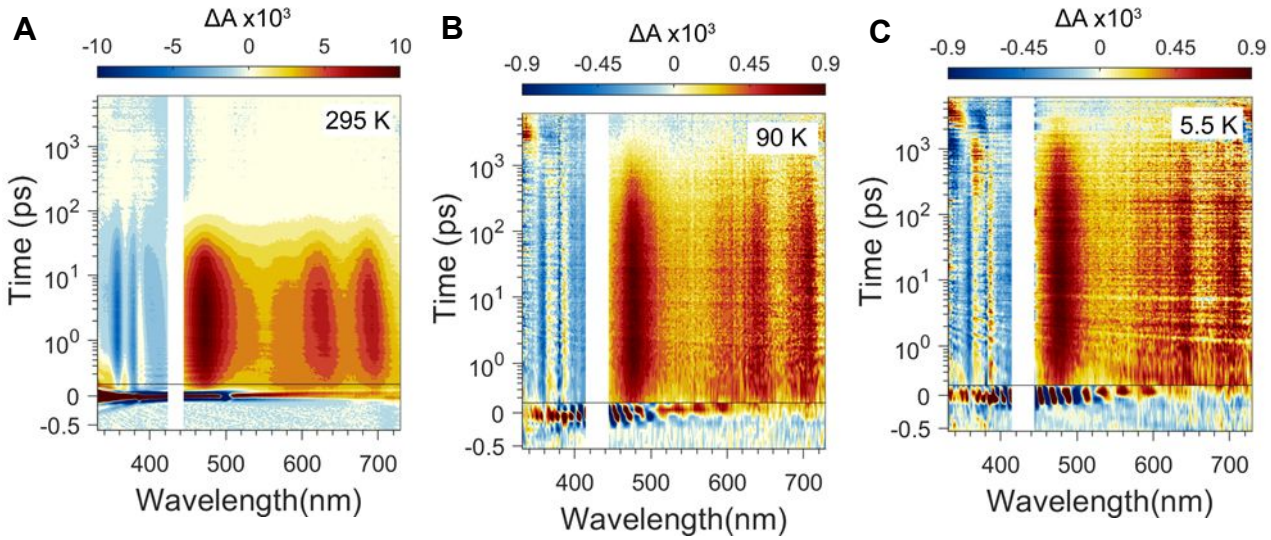

Figure 4. TA spectra **2NDI** in (A) 1,4-dioxane at 295K, (B) glassy Me-THF at 90K, and (C) glassy Me-THF at 5.5K. Upper and lower sections of each plot are displayed with logarithmic and linear scales, respectively. Pump scatter is blocked for clarity.

We quantified the effect of the second **NDI** acceptor on the sub-picosecond CS dynamics seen in Figures 3 and 4 by measuring the CS rate constants k_{CS} for both **1NDI** and **2NDI** and then evaluating the ratio k_{CS}(**2NDI**)/k_{CS}(**1NDI**). We conducted global fitting analyses of the most prominent anionic TA ESA feature at 475 nm for both **1NDI** and **2NDI** where group velocity mismatch between the pump and probe did not significantly stretch the time resolution τ_{IRF} of the experiment. CS was assumed to be a first-order kinetic process, so the kinetic traces were fit to a

sum of exponential decays (see SI-1.4). The CS rates extracted from these analyses are tabulated in Table 2; these values represent the average CS rate constant from measurements made on three days along with one standard deviation, $\langle k_{CS} \rangle \pm \sigma$. CS rate constants in these experiments were measured to range between $(200 \pm 20 \text{ fs})^{-1}$ and $(890 \pm 20 \text{ fs})^{-1}$, the most rapid of which are still resolvable with the about 90 fs τ_{IRF} of our experiments. As the temperature was decreased, we observed a corresponding decrease in the CS rate constant for both **1NDI** and **2NDI**.

Table 2. Charge separation and charge recombination rate constants determined from global fitting of the short and long-time TA data, respectively, for **1NDI** and **2NDI** along with the ratio of **2NDI** rate constants to those of **1NDI**.

	k_{CS} (fs^{-1})			k_{CR} (ps^{-1})		
	295 K 1,4-dioxane	90 K Me-THF	5.5 K Me-THF	295 K 1,4-dioxane	90 K Me-THF	5.5 K Me-THF
1NDI	$(410 \pm 20)^{-1}$	$(580 \pm 60)^{-1}$	$(890 \pm 20)^{-1}$	$(25 \pm 2)^{-1}$	$(1407 \pm 7)^{-1}$	$(1800 \pm 100)^{-1}$
2NDI	$(200 \pm 20)^{-1}$	$(240 \pm 20)^{-1}$	$(340 \pm 30)^{-1}$	$(32 \pm 2)^{-1}$	$(690 \pm 50)^{-1}$	$(1100 \pm 200)^{-1}$
Rate Ratio	2.1 ± 0.2	2.4 ± 0.3	2.6 ± 0.2	0.8 ± 0.1	2.0 ± 0.2	1.7 ± 0.3

To investigate the involvement of coherence in electron transfer within these single- and dual-acceptor systems, we evaluated the ratio of the **2NDI** to **1NDI** CS rate constants k_{CS}(**2NDI**)/k_{CS}(**1NDI**) at each temperature. These ratios along with one standard deviation are given in Table 2. At 295K in 1,4-dioxane, k_{CS}(**2NDI**)/k_{CS}(**1NDI**) is within experimental error of two whereas at cryogenic temperatures in glassy Me-THF k_{CS}(**2NDI**)/k_{CS}(**1NDI**) rises above two, specifically to 2.4 ± 0.3 at 90 K and of 2.6 ± 0.2 at 5.5 K. Figure 5 shows example kinetic traces at a probe wavelength of 477 nm (**NDI**$^{\bullet-}$ peak maximum), produced from the average of three experimental trials, for both **1NDI** and **2NDI**. The solid lines and shading represent the average fit

along with one standard deviation. Refer to Figure S4 for example fits at all experimental conditions. Shifting and normalization of these data and fit traces illustrates the deviation of k_{CS}(**2NDI)** from twice that of **1NDI** (dashed line shown in Figure 5).

To better understand the role of electronic coherence and dephasing in electron transfer, we examine our results within the framework of the spin-boson model.[70,71] There are three distinct physical scenarios depending on the nature of the interaction between the **DMA** donor and two **NDI** acceptors and between the two **NDI** acceptors and the bath, assuming nonadiabatic ET, weak system-bath coupling, and fast relaxation of the bath modes (see SI-3).[71] In scenario (I) molecular vibrations or interactions with the solvent disrupt the equivalency of the two **NDI** acceptors and k_{CS}(**2NDI**)/k_{CS}(**1NDI**) = 2; this is the incoherent scenario. In scenario (II) the two **NDI** acceptors remain equivalent but the bosonic bath modes are over-damped giving k_{CS}(**2NDI**)/k_{CS}(**1NDI**) < 2 with the high-temperature limit yielding k_{CS}(**2NDI**)/k_{CS}(**1NDI**) = 1; this is the coherent, over-damped scenario. In scenario (III) the two **NDI** acceptors are equivalent and the bosonic bath modes are under-damped giving k_{CS}(**2NDI**)/k_{CS}(**1NDI**) >2 with the low-temperature limit yielding k_{CS}(**2NDI**)/k_{CS}(**1NDI**) = 4; this is the constructive coherent limit.

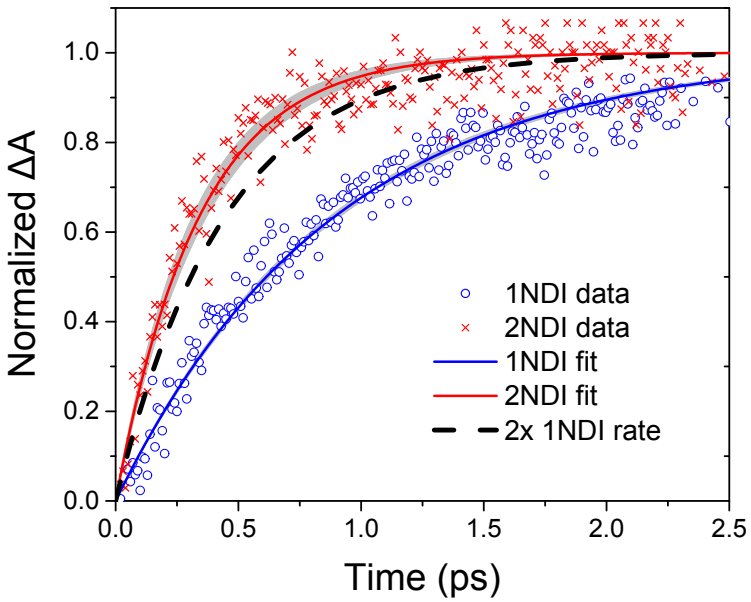

Figure 5. Normalized kinetic traces and fits at the 477 nm probe wavelength for **1NDI** (blue) and **2NDI** (red) in glassy Me-THF at 5.5 K along with a curve illustrating twice the CS rate (dashed black) found for the **1NDI** compound. Uncertainty in the fits shown here represents the standard deviation in the CS rate constants found for measurements made on three separate days. To aid direct comparison, we shifted both the data and the fits to intersect at the origin and subsequently normalized all traces from 0 to 1.

The value of k_{CS}(**2NDI**)/k_{CS}(**1NDI**) determined for CS in 1,4-dioxane at 295 K is indistinguishable from that described by the incoherent scenario (I) given the experimental error. This is expected since thermal motion at room temperature allows for dynamic solvent environments and molecular vibrations that can lead to uncorrelated fluctuations in the energies of the two **NDI** acceptors. As a result, the two **NDI**s couple as distinct, non-interacting sites to the donor and k_{CS} increases by a factor of 2. As the temperature is decreased, and specifically as the solvent freezes, the determined values of k_{CS}(**2NDI**)/k_{CS}(**1NDI**) increase to be statistically greater than 2, indicating a transition from the incoherent scenario (I) to the constructive coherent scenario (III). The observed values of k_{CS}(**2NDI**)/k_{CS}(**1NDI**) > 2 are unlikely to be caused by changes in ΔG_{CS} or λ. As discussed earlier, at low temperatures CS is in the Marcus-inverted region and,

furthermore, λ for **2NDI** decreases compared to **1NDI** while ΔG_{CS} is slightly more favorable for **2NDI** than **1NDI**. Thus, based on ΔG_{CS} and λ alone, and excluding the statistical factor of 2 enhancement, one would expect k_{CS} to decrease, not increase. Instead, the frozen solvent likely shields the two acceptors from the rapid fluctuations present at ambient conditions resulting in longer correlations between the energies of the two **NDI**s so that they couple coherently to the donor state. In this scenario, it becomes more convenient to consider the superposition states $A_{+/-} = (|\boldsymbol{NDI_1}> \pm |\boldsymbol{NDI_2}>)/\sqrt{2}$ which couple to the donor state with $V_{+/-} = (V_{DA} \pm V_{DA})/\sqrt{2}$. Here $|\boldsymbol{NDI_1}>$ and $|\boldsymbol{NDI_2}>$ represent the acceptor states of the two equivalent **NDI** moieties as shown in Scheme 1, V_{DA} is the coupling between the donor and a single acceptor, and $V_{+/-}$ is the renormalized coupling between the donor and the $A_{+/-}$ superposition states. Scheme 1 indicates how coupling between the two **NDI** moieties in **2NDI** causes the A_+ state to be stabilized and the A_- state to be destabilized with respect to the original **NDI** energy levels. This treatment demonstrates how the antibonding state A_- is uncoupled from the donor while the bonding state A_+ has an increased coupling of $\sqrt{2}V_{DA}$. In the same manner that the coupling between A_+ and the donor is renormalized by a factor of $\sqrt{2}$, the coupling between A_+ and the bath V_{SB} should also be renormalized by a factor of $\sqrt{2}$. In the context of the spin-boson model, ET in a system that interacts only weakly with the bath, which has fast relaxation, can be approximated with Equation 5

$$k_{ET} \approx (V_{DA}^2 \kappa)/(\kappa^2 + \varepsilon_{DA}^2) \qquad \text{Equation 5}$$

where V_{DA} is the donor-acceptor coupling, κ is a dephasing parameter that is proportional to V_{SB}^2, and ε_{DA} is the instantaneous DA energy gap (see SI-3).[71] At low enough temperatures $\kappa << \varepsilon_{DA}$ and Equation 5 reduces to $k_{ET} \approx (V_{DA}^2\kappa)/\varepsilon_{DA}^2$ indicating that, since V_{DA} and V_{SB} are both renormalized by a factor of $\sqrt{2}$, k_{ET} can be enhanced by up to a factor of 4 via the presence of the

second acceptor in the constructive coherent limit, i.e. k_{CS}(**2NDI**)/k_{CS}(**1NDI**) = 4. The observed ratios at cryogenic temperatures clearly do not show a factor of four enhancement, which indicates that the assumption $\kappa << \varepsilon_{DA}$ is not completely valid even at 5.5 K. Physically, this suggests that the energy fluctuations of the two **NDI**s are still large enough to lead to dephasing on the CS timescale which manifests as a ratio statistically larger than 2 but not reaching the factor of 4 limit. The source of dephasing here could be due to low frequency modes of the acceptors or interaction between the bath and the relatively large aromatic surface or alkyl solubilizing tail. Regardless, these results highlight the importance of controlling the system-bath interactions in a manner that minimizes dephasing. While shielding the acceptors from dephasing is achieved here to a small degree by drastically decreasing the temperature, it is similar to the proposed role of the protein matrix in PS that enables relatively long lifetimes for vibrational coherences.[18,20,50]

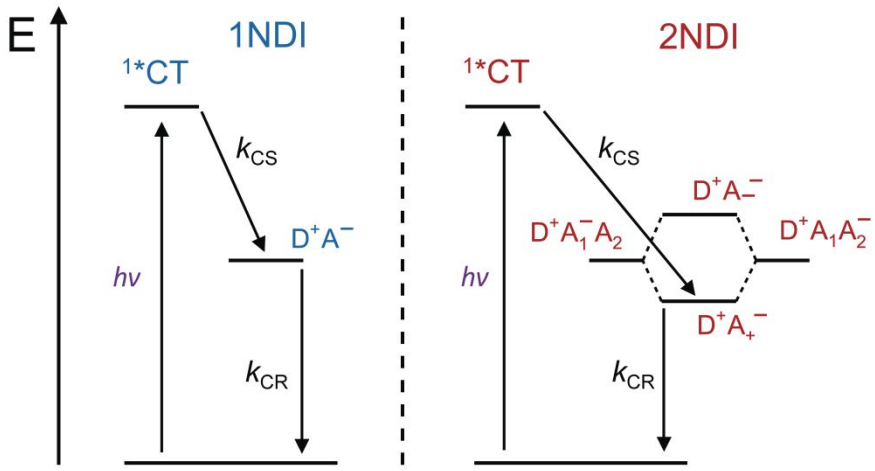

Scheme 1. Jablonski diagram showing the relevant states and processes (i.e. population flow) in **1NDI** (left) and **2NDI** (right) at cryogenic temperatures where the two acceptors A_1 and A_2 couple to form the bonding A_+ and antibonding A_- states. Local triplet levels are suppressed from this diagram for clarity.

3.5.2 Charge recombination dynamics

The **DMA$^{\bullet+}$-An-NDI$^{\bullet-}$** ESA decays on the tens of picoseconds timescale for both **1NDI** and **2NDI** in 1,4-dioxane at 295 K as can be seen in Figures 3A and 4A, respectively. Following the decay of the RP state, a weak absorption persists on the nanosecond timescale. At cryogenic temperatures, the **DMA$^{\bullet+}$-An-NDI$^{\bullet-}$** ESA shows a marked increase in lifetime with respect to that at room temperature from the tens of picoseconds to single nanosecond timescale (Figures 3-4). There is again a weak absorption that persists after the RP signal has decayed completely. At all temperatures, the absorption of this final state is too weak to interpret, though, given the energy of the RP state it is possible that it results from a fraction of the **DMA$^{\bullet+}$-An-NDI$^{\bullet-}$** population undergoing CR to a local triplet state, e.g. **^{3*}NDI**, via an enhanced intersystem crossing mechanism.[72] While the absorption of this state could not be interpreted, it was accounted for in the kinetic fits to ensure that it did not impact the extracted CR rate constants, k_{CR}. Additionally, the TA spectra shown in Figures 3 and 4 indicate a clear enhancement in the charge recombination at cryogenic temperatures for **2NDI** compared to **1NDI**, but not at room temperature.

To quantify the apparent differences in k_{CR} between **1NDI** and **2NDI** we conducted global fitting analyses (i) on the TA data collected at 295 K using the same method as for k_{CS} and (ii) on the TA data collected at 90 and 5.5 K using a multi-wavelength global fitting methodology described in the SI. Briefly, the differential equations for the sequential $A \rightarrow B \rightarrow C$ model were solved numerically and the kinetic parameters (e.g. rate constants) that best match the fits to the raw data were determined via least-squares fitting. These parameters were then used to extract population curves for each species which were then used to deconvolute the raw data and extract the evolution-associated spectrum (EAS) for each species. In these fits, we used an extra exponential decay to remove the cross-phase modulation contribution to the TA spectra. Species A, B, and C refer to the initial photoexcited CT state, the RP state, and the weak long-lived ESA

discussed above, respectively. Furthermore, the rate constant for population transfer from A to B, i.e. k_{CS}, was fixed to the values listed in Table 2 and only the rate constant for population transfer from B to C, i.e. k_{CR}, was fit. The left panels of Figures 6 and 7 show the EAS for **1NDI** and **2NDI** at 90 and 5.5 K, respectively, while the right panels provide representative kinetics at probe wavelengths corresponding to key spectral features and the associated fits determined by this method.

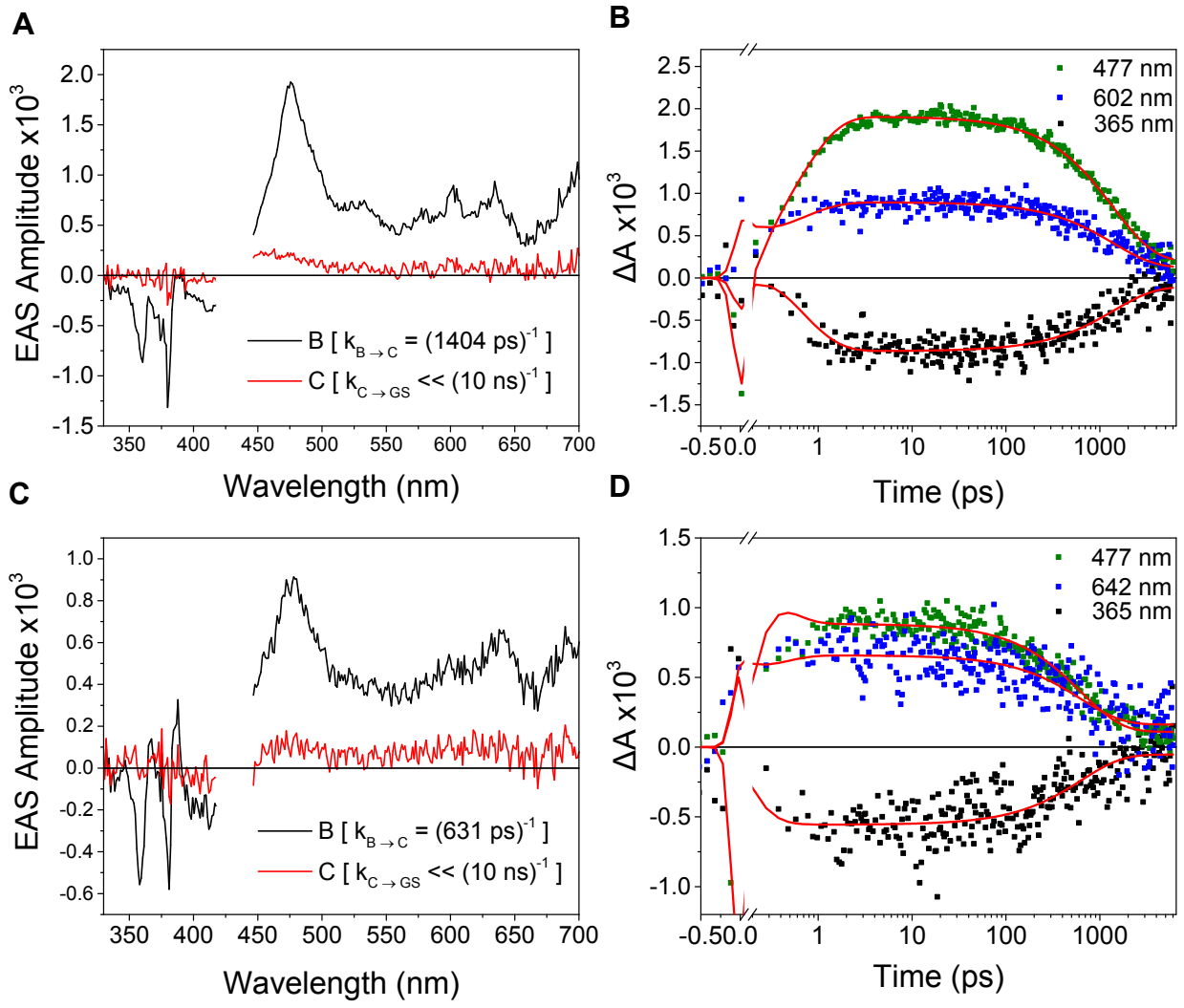

Figure 6. Evolution-associated spectra (left) and selected single-wavelength kinetics (right) for (A and B) **1NDI** in Me-THF at 90 K and (C and D) **2NDI** in Me-THF at 90 K. Rate constants for the processes shown in (A) and (C) are given in parentheses, where GS signifies the terminal ground state of the system.

Through comparison of panels (B) and (D) of both Figures 6 and 7, it is evident that CR, which is predominantly to S_0, is accelerated when two **NDI** moieties are present in contrast to one. Values of k_{CR} determined by our model are given in Table 2 in the right column along with the determined ratio values comparing the CR rate constants for **2NDI** and **1NDI**, k_{CR}(**2NDI**)/k_{CR}(**1NDI**). At both 90 and 5.5 K in glassy Me-THF, we found the value of k_{CR}(**2NDI**)/k_{CR}(**1NDI**) to be 2 within the experimental uncertainty. In contrast, at 295 K in 1,4-dioxane, we found k_{CR}(**2NDI**)/k_{CR}(**1NDI**) to be slightly less than 1. Similar to CS, the changes in k_{CR} are unlikely to stem from shifts in the CR driving force ΔG_{CR} and the CR reorganization energy, λ_{CR}. The values for ΔG_{CR} equal the negative of the energies of the RP states (i.e. $\Delta G_{CR} < -1.77$ eV) and are much larger than the values for λ_{CR}, which are likely similar to those for CS (i.e. $\lambda_{CR} < 1.0$ eV). This demonstrates that CR is also far in the Marcus-inverted region. While ΔG_{CR} is less favorable for **2NDI** than for **1NDI**, λ_{CR} also decreases for **2NDI** and is likely to offset the decreased ΔG_{CR}. This conclusion is further supported by the large differences observed for k_{CR}(**2NDI**)/k_{CR}(**1NDI**) at room and cryogenic temperatures since the relative changes in ΔG_{CR} and λ_{CR} between **1NDI** and **2NDI** are similar in both temperature regimes. Instead, these k_{CR} ratio values are consistent with the CS observations and proposed models describing the interaction of the donor, two acceptors, and bath. At 295 K in 1,4-dioxane, we found k_{CS}(**2NDI**)/k_{CS}(**1NDI**) to be about 2 and attributed that to rapid fluctuations of the energies of the two **NDI** acceptors causing them to couple distinctly to the donor. Since, in this scenario, CS occurs to individual acceptor moieties, the electron likely remains localized on a single acceptor until CR occurs. If the electron only interacts with a single acceptor, then the presence of the second acceptor should have no effect and k_{CR}(**2NDI**)/k_{CR}(**1NDI**) = 1. The deviation to a value slightly less than 1 could indicate that the electron is hopping between

acceptors on a similar timescale than that of CR, a phenomenon we have previously found to decrease the CR rate.[73] At 90 and 5.5 K in Me-THF, we observed k_{CS}(**2NDI**)/k_{CS}(**1NDI**) > 2, providing evidence that CS occurs to a superposition of the two acceptors. If the electron remains in this delocalized superposition state for a timescale longer than that of CR, then the DA coupling for the CR reaction will again be renormalized by a factor of $\sqrt{2}$, contributing a factor of 2 increase to k_{CR}(**2NDI**) compared to k_{CR}(**1NDI**). The nature of the system-bath interactions is less clear here, though two plausible explanations are as follows: (i) the timescale of CR and the temperature place the system at an intermediate state between the under- and over-damped scenarios and (ii) CR is again predominantly driven by system-bath coupling via the acceptor, which in the CR reaction is **DMA**$^{\bullet+}$. In this case there is no renormalization of the system-bath coupling upon addition of the second acceptor so CR in **2NDI** is limited to twice the rate of CR in **1NDI**.

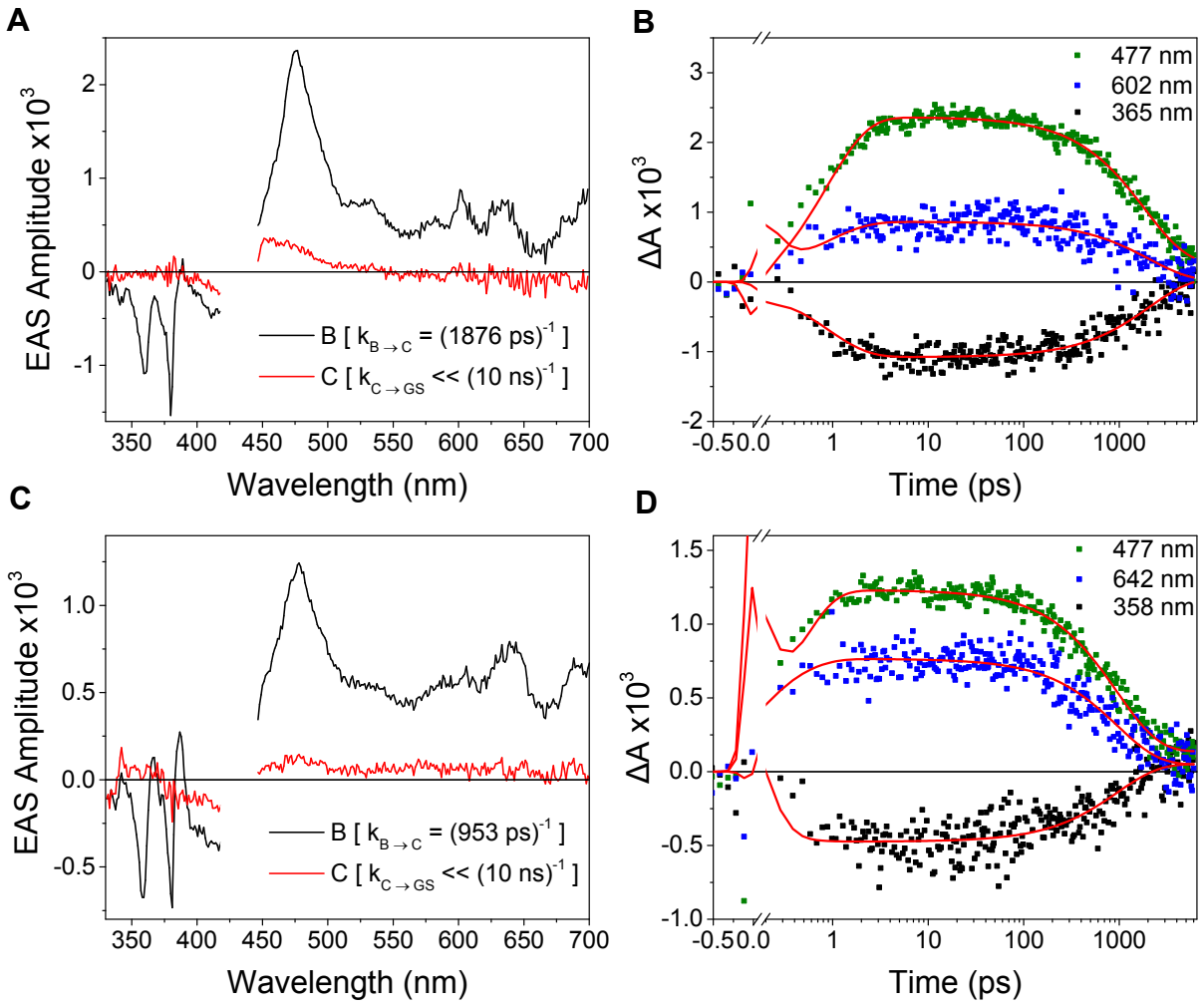

Figure 7. Evolution-associated spectra (left) and selected single-wavelength kinetics (right) for (A and B) **1NDI** in Me-THF at 5.5 K and (C and D) **2NDI** in Me-THF at 5.5 K. Rate constants for the processes shown in (A) and (C) are given in parentheses, where GS signifies the terminal ground state of the system.

4. Conclusion

The DA molecules reported here, **1NDI** and **2NDI**, were synthesized to probe the role of electronic coherence between two equivalent acceptor sites and the resultant impact on electron transfer rates. Following excitation to an intramolecular CT state, both compounds exhibit CS with sub-picosecond rate constants ranging between $(890\ fs)^{-1}$ and $(200\ fs)^{-1}$ followed by CR with rate constants ranging from $(25\ ps)^{-1}$ in 1,4-dioxane at 295 K to $(1800\ ps)^{-1}$ in Me-THF at 5.5 K.

Comparison of the rate constants for **2NDI** and **1NDI** indicated that transitioning from a room temperature solution to a frozen matrix lead to non-statistical enhancement in the CS rate constant, with a small effect observed just below the glassing temperature and a larger effect observed near liquid helium temperatures. When system-bath interactions are considered in the context of the spin-boson model, the transition from a statistical CS rate enhancement at room temperature to greater-than-statistical rate enhancement at cryogenic temperatures can be attributed to a change in the magnitude of the fluctuations experienced by the two acceptor sites. At cryogenic temperatures, reduced fluctuations enable the two acceptors in **2NDI** to remain coherent for longer timescales where CS likely occurs to a superposition state of the two acceptors. Furthermore, coupling between this superposition state and the bath pushes the rate enhancement beyond the statistical limit. The observed CS and CR dynamics have been explained in the context of this model and demonstrate the importance of shielding the system from randomizing fluctuations if observing or manipulating coherences is desired, which is in concert with current explanations for long-lived coherences in protein matrices or the solid state. Though **2NDI** demonstrated the effects of coherent interactions, the fully coherent limit was not observed and further studies looking at other acceptors with different solubilizing groups or structures could provide additional insight into the precise source of the dephasing in these and related systems.

5. References

1. Scholes GD, Fleming GR, Chen LX, Aspuru-Guzik A, Buchleitner A, Coker DF, et al. Using coherence to enhance function in chemical and biophysical systems. Nature. 2017;543:647.

2. Savikhin S, Buck DR, Struve WS. Oscillating anisotropies in a bacteriochlorophyll protein: Evidence for quantum beating between exciton levels. Chemical Physics. 1997;223(2):303-312.

3. Cheng Y-C, Fleming GR. Dynamics of Light Harvesting in Photosynthesis. Annual Review of Physical Chemistry. 2009;60(1):241-262.

4. Engel GS, Calhoun TR, Read EL, Ahn T-K, Mančal T, Cheng Y-C, et al. Evidence for wavelike energy transfer through quantum coherence in photosynthetic systems. Nature. 2007;446:782.

5. Chenu A, Scholes GD. Coherence in Energy Transfer and Photosynthesis. Annual Review of Physical Chemistry. 2015;66(1):69-96.

6. Collini E, Scholes GD. Coherent Intrachain Energy Migration in a Conjugated Polymer at Room Temperature. Science. 2009;323(5912):369.

7. Musser AJ, Liebel M, Schnedermann C, Wende T, Kehoe TB, Rao A, et al. Evidence for conical intersection dynamics mediating ultrafast singlet exciton fission. Nature Physics. 2015;11:352.

8. Mirjani F, Renaud N, Gorczak N, Grozema FC. Theoretical Investigation of Singlet Fission in Molecular Dimers: The Role of Charge Transfer States and Quantum Interference. The Journal of Physical Chemistry C. 2014;118(26):14192-14199.

9. Skourtis SS, Beratan DN, Waldeck DH. Coherence in electron transfer pathways. Procedia Chemistry. 2011;3(1):99-104.

10. Bakulin AA, Rao A, Pavelyev VG, van Loosdrecht PHM, Pshenichnikov MS, Niedzialek D, et al. The Role of Driving Energy and Delocalized States for Charge Separation in Organic Semiconductors. Science. 2012;335(6074):1340.

11. Falke SM, Rozzi CA, Brida D, Maiuri M, Amato M, Sommer E, et al. Coherent ultrafast charge transfer in an organic photovoltaic blend. Science. 2014;344(6187):1001.

12. Andrea Rozzi C, Maria Falke S, Spallanzani N, Rubio A, Molinari E, Brida D, et al. Quantum coherence controls the charge separation in a prototypical artificial light-harvesting system. Nature Communications. 2013;4:1602.

13. Song Y, Clafton SN, Pensack RD, Kee TW, Scholes GD. Vibrational coherence probes the mechanism of ultrafast electron transfer in polymer–fullerene blends. Nature Communications. 2014;5:4933.

14. Rury AS, Sorenson SA, Dawlaty JM. Coherent Vibrational Probes of Hydrogen Bond Structure Following Ultrafast Electron Transfer. The Journal of Physical Chemistry C. 2016;120(38):21740-21750.

15. Rafiq S, Scholes GD. From Fundamental Theories to Quantum Coherences in Electron Transfer. Journal of the American Chemical Society. 2018.

16. Fuller FD, Pan J, Gelzinis A, Butkus V, Senlik SS, Wilcox DE, et al. Vibronic coherence in oxygenic photosynthesis. Nature Chemistry. 2014;6:706.

17. Ruhman S, Joly AG, Nelson KA. Coherent molecular vibrational motion observed in the time domain through impulsive stimulated Raman scattering. IEEE Journal of Quantum Electronics. 1988;24(2):460-469.

18. Lee H, Cheng Y-C, Fleming GR. Coherence Dynamics in Photosynthesis: Protein Protection of Excitonic Coherence. Science. 2007;316(5830):1462.

19. Fang C, Frontiera RR, Tran R, Mathies RA. Mapping GFP structure evolution during proton transfer with femtosecond Raman spectroscopy. Nature. 2009;462:200.

20. Panitchayangkoon G, Hayes D, Fransted KA, Caram JR, Harel E, Wen J, et al. Long-lived quantum coherence in photosynthetic complexes at physiological temperature. Proceedings of the National Academy of Sciences. 2010;107(29):12766.

21. Vos MH, Jones MR, Hunter CN, Breton J, Martin JL. Coherent nuclear dynamics at room temperature in bacterial reaction centers. Proceedings of the National Academy of Sciences. 1994;91(26):12701.

22. Vos MH, Jones MR, Hunter CN, Breton J, Lambry J-C, Martin J-L. Coherent Dynamics during the Primary Electron-Transfer Reaction in Membrane-Bound Reaction Centers of Rhodobacter sphaeroides. Biochemistry. 1994;33(22):6750-6757.

23. Vos MH, Rappaport F, Lambry J-C, Breton J, Martin J-L. Visualization of coherent nuclear motion in a membrane protein by femtosecond spectroscopy. Nature. 1993;363:320.

24. Duan H-G, Prokhorenko VI, Cogdell RJ, Ashraf K, Stevens AL, Thorwart M, et al. Nature does not rely on long-lived electronic quantum coherence for photosynthetic energy transfer. Proceedings of the National Academy of Sciences of the United States of America. 2017;114(32):8493-8498.

25. Fassioli F, Dinshaw R, Arpin PC, Scholes GD. Photosynthetic light harvesting: excitons and coherence. Journal of The Royal Society Interface. 2014;11(92).

26. Lewis FD, Zhu H, Daublain P, Fiebig T, Raytchev M, Wang Q, et al. Crossover from Superexchange to Hopping as the Mechanism for Photoinduced Charge Transfer in DNA Hairpin Conjugates. Journal of the American Chemical Society. 2006;128(3):791-800.

27. Goldsmith RH, Sinks LE, Kelley RF, Betzen LJ, Liu W, Weiss EA, et al. Wire-like charge transport at near constant bridge energy through fluorene oligomers. Proceedings of the National Academy of Sciences of the United States of America. 2005;102(10):3540.

28. Davis WB, Ratner MA, Wasielewski MR. Conformational Gating of Long Distance Electron Transfer through Wire-like Bridges in Donor−Bridge−Acceptor Molecules. Journal of the American Chemical Society. 2001;123(32):7877-7886.

29. McConnell HM. Intramolecular Charge Transfer in Aromatic Free Radicals. The Journal of Chemical Physics. 1961;35(2):508-515.

30. Kilså K, Kajanus J, Macpherson AN, Mårtensson J, Albinsson B. Bridge-Dependent Electron Transfer in Porphyrin-Based Donor−Bridge−Acceptor Systems. Journal of the American Chemical Society. 2001;123(13):3069-3080.

31. Reimers JR, Hush NS. Spectroscopic evidence for electronically forbidden but vibronically allowed long-range electron transfer in norbornylog-bridged naphthalene-diacyanoethylene systems. Chemical Physics. 1990;146(1):105-114.

32. Reimers JR, Hush NS, Sammeth DM, Callis PR. Two-photon fluorescence excitation spectrum of a naphthalene norbornylog: Implications for electron transfer. Chemical Physics Letters. 1990;169(6):622-626.

33. Zeng Y, Zimmt MB. Symmetry Effects in Photoinduced Electron-Transfer Reactions. Journal of the American Chemical Society. 1991;113(13):5107-5109.

34. Zeng Y, Zimmt MB. Symmetry effects on electron-transfer reactions: temperature dependence as a diagnostic tool. The Journal of Physical Chemistry. 1992;96(21):8395-8403.

35. Garner MH, Solomon GC, Strange M. Tuning Conductance in Aromatic Molecules: Constructive and Counteractive Substituent Effects. The Journal of Physical Chemistry C. 2016;120(17):9097-9103.

36. Solomon GC, Andrews DQ, Goldsmith RH, Hansen T, Wasielewski MR, Van Duyne RP, et al. Quantum Interference in Acyclic Systems: Conductance of Cross-Conjugated Molecules. Journal of the American Chemical Society. 2008;130(51):17301-17308.

37. Maggio E, Solomon GC, Troisi A. Exploiting Quantum Interference in Dye Sensitized Solar Cells. ACS Nano. 2014;8(1):409-418.

38. Huang G-J, Harris MA, Krzyaniak MD, Margulies EA, Dyar SM, Lindquist RJ, et al. Photoinduced Charge and Energy Transfer within meta- and para-Linked Chlorophyll a-Perylene-3,4:9,10-bis(dicarboximide) Donor–Acceptor Dyads. The Journal of Physical Chemistry B. 2016;120(4):756-765.

39. Ricks AB, Solomon GC, Colvin MT, Scott AM, Chen K, Ratner MA, et al. Controlling Electron Transfer in Donor−Bridge−Acceptor Molecules Using Cross-Conjugated Bridges. Journal of the American Chemical Society. 2010;132(43):15427-15434.

40. Beratan DN, Hopfield JJ. Calculation of tunneling matrix elements in rigid systems: mixed-valence dithiaspirocyclobutane molecules. Journal of the American Chemical Society. 1984;106(6):1584-1594.

41. Onuchic JN, Beratan DN. Molecular bridge effects on distant charge tunneling. Journal of the American Chemical Society. 1987;109(22):6771-6778.

42. Curtiss LA, Naleway CA, Miller JR. Superexchange Pathway Calculation of Electronic Coupling through Cyclohexane Spacers. The Journal of Physical Chemistry. 1995;99(4):1182-1193.

43. Goldsmith RH, Wasielewski MR, Ratner MA. Scaling Laws for Charge Transfer in Multiply Bridged Donor/Acceptor Molecules in a Dissipative Environment. Journal of the American Chemical Society. 2007;129(43):13066-13071.

44. Renaud N, Powell D, Zarea M, Movaghar B, Wasielewski MR, Ratner MA. Quantum Interferences and Electron Transfer in Photosystem I. The Journal of Physical Chemistry A. 2013;117(29):5899-5908.

45. Zarea M, Powell D, Renaud N, Wasielewski MR, Ratner MA. Decoherence and Quantum Interference in a Four-Site Model System: Mechanisms and Turnovers. The Journal of Physical Chemistry B. 2013;117(4):1010-1020.

46. Skourtis SS, Waldeck DH, Beratan DN. Inelastic Electron Tunneling Erases Coupling-Pathway Interferences. The Journal of Physical Chemistry B. 2004;108(40):15511-15518.

47. Goldsmith RH, Wasielewski MR, Ratner MA. Electron Transfer in Multiply Bridged Donor−Acceptor Molecules: Dephasing and Quantum Coherence. The Journal of Physical Chemistry B. 2006;110(41):20258-20262.

48. Xiao D, Skourtis SS, Rubtsov IV, Beratan DN. Turning Charge Transfer On and Off in a Molecular Interferometer with Vibronic Pathways. Nano Letters. 2009;9(5):1818-1823.

49. Kumar K, Kurnikov IV, Beratan DN, Waldeck DH, Zimmt MB. Use of Modern Electron Transfer Theories To Determine Electronic Coupling Matrix Elements in Intramolecular Systems. The Journal of Physical Chemistry A. 1998;102(28):5529-5541.

50. Mohseni M, Rebentrost P, Lloyd S, Aspuru-Guzik A. Environment-assisted quantum walks in photosynthetic energy transfer. The Journal of Chemical Physics. 2008;129(17):174106.

51. Skourtis SS, Waldeck DH, Beratan DN. Fluctuations in Biological and Bioinspired Electron-Transfer Reactions. Annual Review of Physical Chemistry. 2010;61(1):461-485.

52. Lin Z, Lawrence CM, Xiao D, Kireev VV, Skourtis SS, Sessler JL, et al. Modulating Unimolecular Charge Transfer by Exciting Bridge Vibrations. Journal of the American Chemical Society. 2009;131(50):18060-18062.

53. Delor M, Archer SA, Keane T, Meijer AJHM, Sazanovich IV, Greetham GM, et al. Directing the path of light-induced electron transfer at a molecular fork using vibrational excitation. Nature Chemistry. 2017;9:1099.

54. Li Z, Smeu M, Rives A, Maraval V, Chauvin R, Ratner MA, et al. Towards graphyne molecular electronics. Nature Communications. 2015;6:6321.

55. Vazquez H, Skouta R, Schneebeli S, Kamenetska M, Breslow R, Venkataraman L, et al. Probing the conductance superposition law in single-molecule circuits with parallel paths. Nature Nanotechnology. 2012;7:663.

56. Richert S, Cremers J, Kuprov I, Peeks MD, Anderson HL, Timmel CR. Constructive quantum interference in a bis-copper six-porphyrin nanoring. Nature Communications. 2017;8:14842.

57. Young RM, Dyar SM, Barnes JC, Juríček M, Stoddart JF, Co DT, et al. Ultrafast Conformational Dynamics of Electron Transfer in ExBox4+⊂Perylene. The Journal of Physical Chemistry A. 2013;117(47):12438-12448.

58. Shao Y, Gan Z, Epifanovsky E, Gilbert ATB, Wormit M, Kussmann J, et al. Advances in molecular quantum chemistry contained in the Q-Chem 4 program package. Molecular Physics. 2015;113(2):184-215.

59. Gosztola D, Niemczyk MP, Svec W, Lukas AS, Wasielewski MR. Excited Doublet States of Electrochemically Generated Aromatic Imide and Diimide Radical Anions. The Journal of Physical Chemistry A. 2000;104(28):6545-6551.

60. Okada T, Fujita T, Kubota M, Masaki S, Mataga N, Ide R, et al. Intramolecular electron donor-acceptor interactions in the excited state of (anthracene)-(CH2)n-(N,N-dimethylaniline) systems. Chemical Physics Letters. 1972;14(5):563-568.

61. Okada T, Mataga N, Baumann W, Siemiarczuk A. Picosecond laser spectroscopy of 4-(9-anthryl)-N,N-dimethylaniline and related compounds. The Journal of Physical Chemistry. 1987;91(17):4490-4495.

62. Kasha M, Rawls HR, Ashraf El-Bayoumi M. The exciton model in molecular spectroscopy. Pure and Applied Chemistry1965. p. 371.

63. Wu Y, Frasconi M, Gardner DM, McGonigal PR, Schneebeli ST, Wasielewski MR, et al. Electron Delocalization in a Rigid Cofacial Naphthalene-1,8:4,5-bis(dicarboximide) Dimer. Angewandte Chemie International Edition. 2014;53(36):9476-9481.

64. Weller A. Photoinduced Electron Transfer in Solution: Exciplex and Radical Ion Pair Formation Free Enthalpies and their Solvent Dependence. Zeitschrift für Physikalische Chemie1982. p. 93.

65. Siemiarczuk A, Ware WR. Complex excited-state relaxation in p-(9-anthryl)-N,N-dimethylaniline derivatives evidenced by fluorescence lifetime distributions. The Journal of Physical Chemistry. 1987;91(13):3677-3682.

66. Hoffman BM, Ratner MA. Reorganization energies and rate constants for electron reactions in glass-forming media and proteins. Inorganica Chimica Acta. 1996;243(1):233-238.

67. Marcus RA. On the theory of electron-transfer reactions. VI. Unified treatment for homogeneous and electrode reactions. J Chem Phys. 1965;43:679-701.

68. CRC Handbook of Chemistry and Physics. 99th ed. Boca Raton, FL, USA: CRC Press/Taylor & Francis; Internet Version 2018.

69. Furutsuka T, Imura T, Kojima T, Kawabe K. Dielectric Constant of 2-Methyltetrahydrofuran. Technology Reports of the Osaka University. 1974;24:367.

70. Nitzan A. Chemical dynamics in condensed phases: relaxation, transfer, and reactions in condensed molecular systems. New York, USA: Oxford University Press; 2006.

71. Zarea M, Ratner MA, Wasielewski MR. Electron transfer in a two-level system within a Cole-Davidson vitreous bath. The Journal of Chemical Physics. 2014;140(2):024110.

72. Dance ZEX, Mickley SM, Wilson TM, Ricks AB, Scott AM, Ratner MA, et al. Intersystem Crossing Mediated by Photoinduced Intramolecular Charge Transfer: Julolidine−Anthracene Molecules with Perpendicular π Systems. The Journal of Physical Chemistry A. 2008;112(18):4194-4201.

73. Young RM, Jensen SC, Edme K, Wu Y, Krzyaniak MD, Vermeulen NA, et al. Ultrafast Two-Electron Transfer in a CdS Quantum Dot–Extended-Viologen Cyclophane Complex. Journal of the American Chemical Society. 2016;138(19):6163-6170.

Conflicts of interest:

There are no conflicts to declare.

Acknowledgements:

We thank Dr. Mehdi Zarea for helpful discussions regarding the role of the bath, Dr. Yilei Wu for performing the differential pulse voltammetry experiments, and Dr. Noah Horwitz for performing the photolysis experiment. **Funding:** This work was supported by the National Science Foundation under grant number DMR-1710104. This material is based upon work supported by the National Science Foundation Graduate Research Fellowship Program under Grant No. DGE-1842165. Any opinions, findings, and conclusions or recommendations expressed in this material are those of the author(s) and do not necessarily reflect the views of the National Science Foundation.

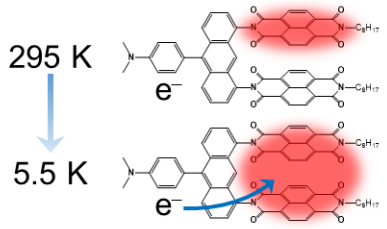

Ultrafast electron transfer occurs with greater-than-statistical rate enhancement at cryogenic temperatures owing to quantum coherence.